J. Iron Steel Res. Int. (2026)33:184
https://doi.org/10.1007/s42243-026-01823-2

ORIGINAL PAPER

# Hydrogen uptake of 100Cr6 bearing steel in gaseous pressurized hydrogen and resulting tensile strength

Maximilian Baur[1] · Iyas Khader[2,1] · Dominik Kürten[1] · Lutz Reißig[1] · Frank Schweizer[1] · Andreas Kailer[1] · Martin Dienwiebel[3]

Received: 19 December 2025 / Revised: 31 March 2026 / Accepted: 3 April 2026


**Abstract**
Samples of martensitic-hardened bearing steel 100Cr6 (AISI 52100) were exposed to hydrogen atmospheres at different gas pressures. The resulting hydrogen contents were measured, and a pressure-dependent hydrogen charging curve was established. Tensile tests on cylindrical specimens charged at various hydrogen pressures showed a pronounced reduction in strength at hydrogen contents as low as $0.75 \times 10^{-6}$. Fractographic analysis revealed predominantly intergranular fracture with crack propagation along carbide-featured grain boundaries, indicating hydrogen enrichment at microstructural traps. Specimens, in which diffusible hydrogen was allowed to outgas prior to testing, largely recovered their initial strength, demonstrating that the observed embrittlement is mainly governed by diffusible hydrogen and is, to a significant extent, reversible. These findings provide insight into the pressure-dependent influence of hydrogen on the strength and reliability of bearing components operating in hydrogen environments.

**Keywords** Hydrogen · Bearing steel · Material property · Trapping energy · Affordable and clean energy

## 1 Introduction

Rolling bearings are indispensable components in many machines and systems. They enable the efficient transmission of forces and are often exposed to high loads. A crucial problem that limits the life of bearings is hydrogen embrittlement. Hydrogen can come into contact with bearing steel for various reasons, e.g., the use of specific lubricants [1–5]. If hydrogen penetrates steel, this can lead to embrittlement-related premature failure [6], which in turn degrades the reliability of bearings. Molecular hydrogen must first dissociate into atomic form before diffusing into the metal lattice. While spontaneous dissociation of $H_2$ molecules is thermodynamically not feasible under typical application conditions, dissociative adsorption at the steel surface enables the formation of atomic hydrogen [7]. These hydrogen atoms can then diffuse into the steel and cause embrittlement. This mechanism is especially relevant for bearing steels in hydrogen compressors, where surface-mediated uptake is critical. Experimental studies confirm that even under gaseous hydrogen atmospheres, significant hydrogen absorption can occur once dissociative adsorption has taken place [8].

The effect of hydrogen embrittlement can be observed particularly in high-strength steels, including bearing steels used in demanding applications such as hydrogen compressors [1, 9–12].

For this reason, it is of great interest to investigate the effects of hydrogen on the material properties of bearing steel. Numerous studies have shown that hydrogen can significantly affect the mechanical properties of bearing steel [1, 11, 12]. Hydrogen embrittlement reduces the fracture toughness and ductility, making the steel more susceptible to crack growth and fracture. In addition, hydrogen can also impair the corrosion resistance of the bearing steel, which can lead to accelerated degradation of

✉ Maximilian Baur
maximilian.baur@iwm.fraunhofer.de

[1] Microtribology Centrum, Fraunhofer Institute for Mechanics of Materials IWM, Freiburg 79108, Germany

[2] Department of Industrial Engineering, German Jordanian University, Amman 11180, Jordan

[3] Institute for Applied Materials – Reliability and Microstructure, Karlsruhe Institute of Technology (KIT), Karlsruhe 76131, Germany

Published online: 21 May 2026

the material. For the austenitic steels with very ductile material behavior, it has been shown that ductility is reduced after exposure to hydrogen [9, 13, 14].

The most famous concepts for the description of hydrogen embrittlement in metals can be divided into two different mechanisms. The first one is hydrogen enhanced local plasticity (HELP): Increased concentrations of hydrogen support the deformation process locally. This effect is triggered by the fact that the hydrogen atoms can be strongly bound in the elastic field around dislocations, thereby reducing the energy required for the dislocation movement [15]. Another hydrogen embrittlement mechanism is called hydrogen enhanced decohesion (HEDE). Here, it is proposed that the strength of the material is weakened by hydrogen occupying grain boundaries and particle–matrix interfaces [16, 17]. It is assumed that the interactions of the two mechanisms, HEDE and HELP, together lead to the effect of hydrogen embrittlement [18, 19]. When investigating the fracture surfaces, intergranular fracture can be observed. As hydrogen accumulates at the grain boundaries, similar to sulfur and phosphorus, it is concluded that the cohesion of grain boundaries is weakened by hydrogen and results in intergranular fracture [20]. In high-strength steels, intergranular fracture due to embrittlement is assumed to be promoted by the pile-up of dislocations and by hydrogen which was carried at grain boundary carbides. The locally enhanced stress leads to the decohesion of the grain boundary and the carbide–matrix interface. Therefore, the synergistic effects of HELP and HEDE result in the intergranular fracture surface [21]. The dislocation movement is enhanced, and the pile-up at grain boundaries leads to the fracture originating at these locations, which can be observed as intergranular fracture with scanning electron microscope (SEM) investigations [22]. Besides, microstructure simulations indicate that the volume in grain boundaries is occupied by hydrogen atoms that lead to the loss of elasticity [23]. Another very important indicator of hydrogen embrittlement is microductile hairlines on the IG fracture surface, so called crow's feet because of their appearance [24, 25]. An important value for assessing the suitability of a material for use in a hydrogen atmosphere is the hydrogen embrittlement susceptibility index (HEI). In very ductile materials, the change in the fracture surface is used as a factor for the evaluation, while for more brittle materials, the elongation at failure is used as a characteristic value [26, 27].

Most past studies on hydrogen embrittlement in high-strength steels have employed electrochemical charging [28, 29]. In contrast, gas charging at controlled pressures allows a broader perspective on embrittlement behavior under practical operating conditions, while avoiding unfavorable surface alteration due to chemical reactions. Both techniques lead to sub-surface hydrogen accumulation in the lattice and reversible trap sites [30]. To gain a better understanding of the behavior of rolling bearings under a hydrogen environment and to increase their reliability, it is therefore crucial to investigate the effect of hydrogen on the mechanical properties of rolling bearing steel in more detail. The results of such investigations can help to improve the development of bearing steels and increase the reliability of bearings in various applications.

It is known that high-strength steels are strongly influenced by the penetration of hydrogen [31–33]. In the case of ductile steel, the necking elongation is reduced. With less ductile steels, however, the strength is even reduced, and failure often occurs in the elastic range before the material's yield strength is reached [33]. In this work, the influence of hydrogen at different pressures on rolling bearing steel is investigated to clarify the resulting effects.

## 2 Materials and methods

### 2.1 Material

Bearing steel 100Cr6 is a high-carbon chromium alloy widely used for rolling elements. Similar samples to those tested in this work were previously analyzed using glow discharge optical emission spectroscopy (GDOES) [4]. The elemental composition is given in Table 1.

The samples were subjected to a controlled heat treatment process to achieve the desired mechanical properties. The tensile samples were austenitized and subsequently hardened under a protective gas atmosphere to minimize oxidation and decarburization. The hardening process was designed to ensure a uniform martensitic microstructure, yielding a final hardness of approximately 58 HRC (Rockwell hardness cone). This treatment yields samples comparable to the through hardened rolling elements. The microstructure of similar bearing steel was analyzed and reported in Šmeļova et al. [34]. The material mainly consisted of tempered martensite, in addition to homogeneously distributed primary spheroidized carbides $(Fe, Cr)_3C$ and tempered carbides. It also included approximately 10%–12% retained austenite.

A comparison of the microstructure of the bearing component and a transverse section of a tensile specimen, both made of 100Cr6 steel, is shown in Fig. 1. The microstructure of the bearing element (Fig. 1a) exhibits slightly finer grain size and higher density of carbides, distributed both along the grain boundaries and within the grains, compared to the tensile sample's microstructure (Fig. 1b). This is consistently observed in optical microscopy as well as in secondary electrons (SE) and backscatter electrons (BSE) microscopy images, where

**Table 1** Elemental composition of bearing steel 100Cr6 (wt.%) [4]

| C | Cr | Mn | Si | Mo | V | Fe |
|---|---|---|---|---|---|---|
| 1.08 ± 0.02 | 1.52 ± 0.03 | 0.33 ± 0.02 | 0.26 ± 0.03 | < 0.1 | < 0.1 | Balance |

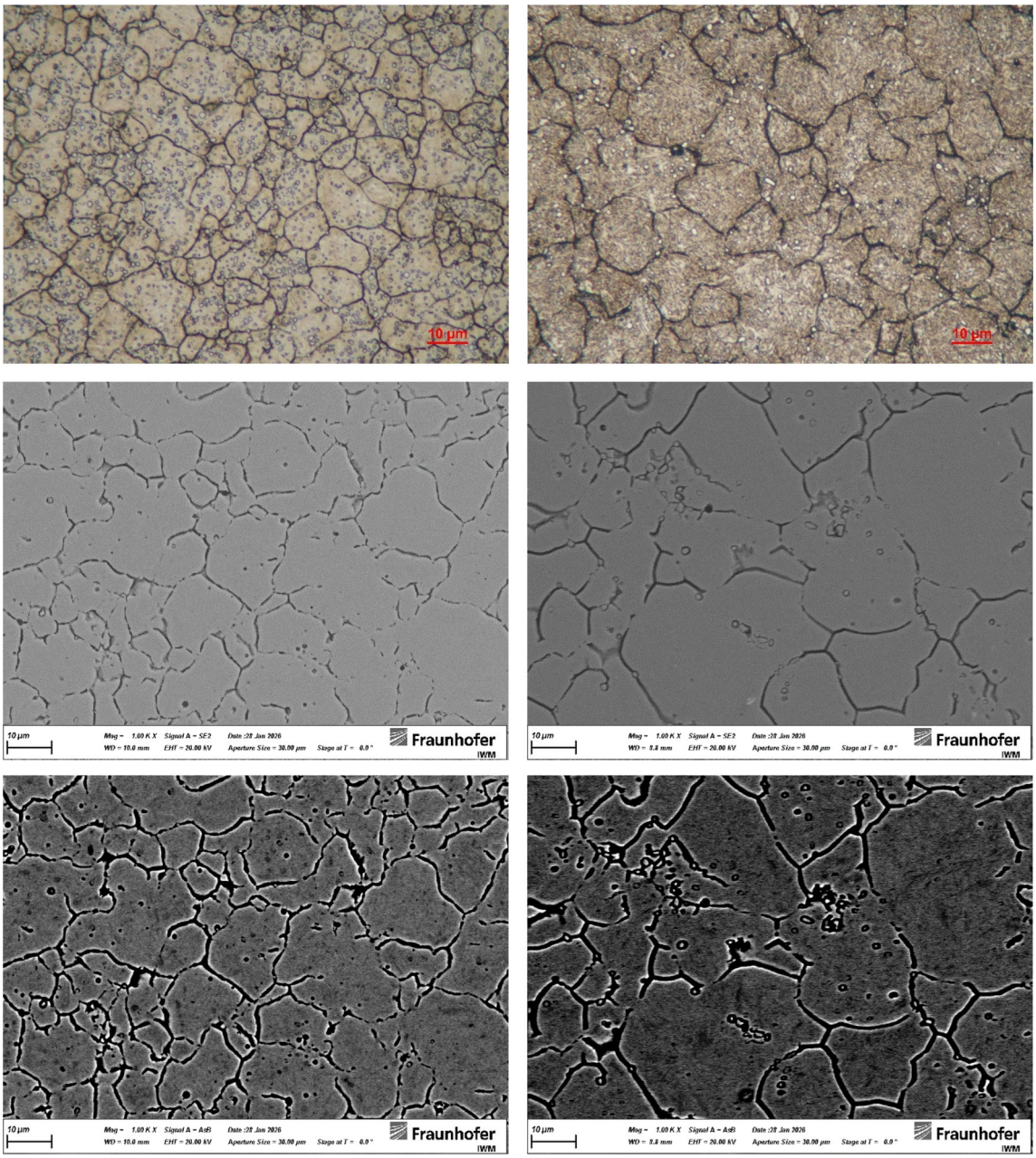


**Fig. 1** Microstructure of a bearing element (**a**) and a transverse section of a tensile sample (**b**) etched under identical conditions: optical microscopy (OM), SE and BSE images from top to bottom

carbides appear with enhanced contrast in the bearing element.

The tensile samples were austenitized at 840 °C for 90 min in a neutral atmosphere (carbon potential 0.8 wt.%)

and oil quenched. Tempering was then carried out in two air furnace cycles. The first cycle was performed at 160 °C for 3 h. The second cycle was performed at 230 °C for 3 h. In each cycle, the furnace was heated from ambient to the setpoint and held isothermally for the stated duration. This customized heat treatment of the tensile samples should result in a comparable microstructure to that of the bearing elements. Nonetheless, the grain size of the tensile specimen still appears slightly coarser than that of the rolling element, as shown in Fig. 1.

Figure 2 shows electron backscatter diffraction (EBSD) results of the investigated 100Cr6 steel tensile samples. The inverse pole figure (IPF) map (Fig. 2a) reveals a fully martensitic microstructure with a lath-like subgrain morphology, indicating prior austenite grain fragmentation. The grain boundary map (Fig. 2b) highlights a high density of high-angle grain boundaries (HAGBs, blue), which dominate the structure (96.2% of total boundaries), while low-angle grain boundaries (LAGBs, red/green) are present in minor fractions. This boundary network suggests a high potential for hydrogen segregation at HAGBs, which are known to promote intergranular decohesion under hydrogen charging conditions. Also, primary carbides are displayed in black, with a diameter of 1–2 µm.

## 2.2 Hydrogen pressure charging

In addition to more accurate process control in terms of hydrogen concentration and more uniform hydrogen distribution within the material, gas pressure charging (unlike electrochemical charging) does not alter surface structure and material properties of the samples. Gas pressure charging was done using a benchtop autoclave (Fig. 3) to expose different types of samples to a hydrogen

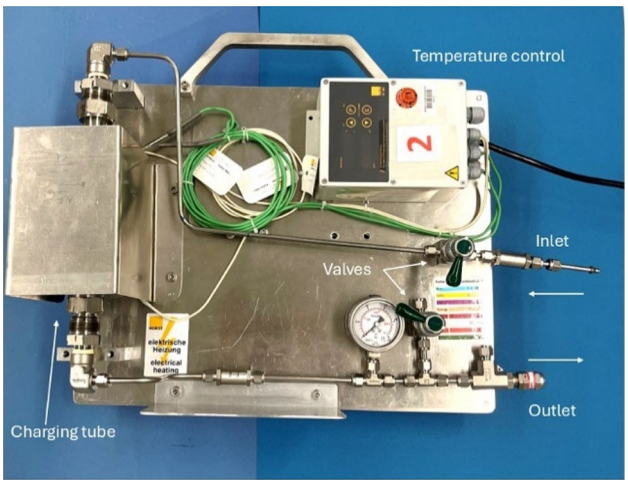


**Fig. 3** Charging chamber for charging samples with pressurized gases

atmosphere. The autoclave allows tempering the samples during the process to allow hydrogen to diffuse into the material. The device is capable of reaching pressures up to 30 MPa and temperatures up to 350 °C.

The autoclave is connected to pressurized cylinders (filled with hydrogen 6.0, up to 20 MPa) using Swagelok fittings. Two ball valves are installed to ensure that no residual ambient atmosphere remains in the autoclave. The pipe section was purged ten times prior to charging to eliminate residual atmospheric gases. This means that the charging pressure is applied and released to a pressure between 1 and 2 MPa via the drain valve. The pressure is measured and displayed via the pressure gauge. The temperature is measured with a PT100 thermocouple, and the temperature is controlled using a temperature controller.

Charging was done to create pressure-dependent charging curves and to pre-charge tensile samples. The

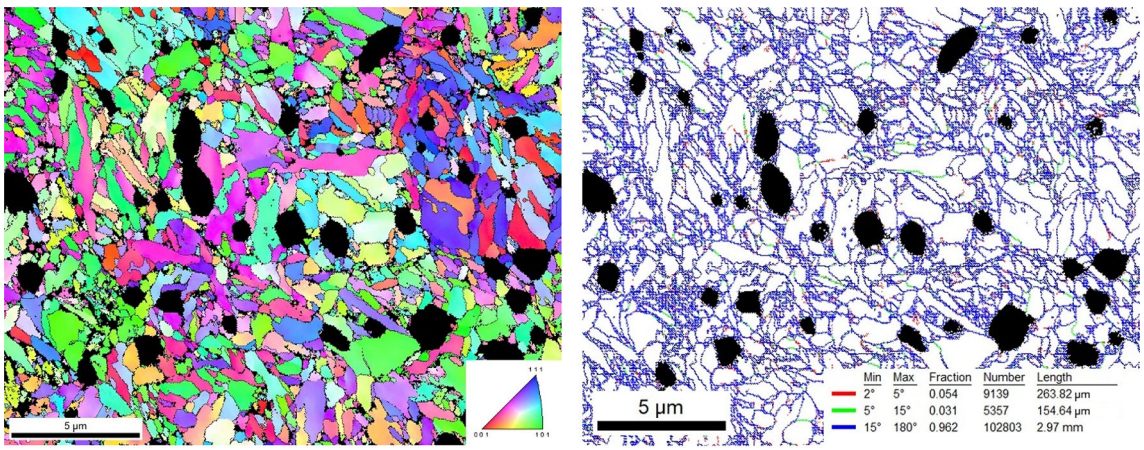


**Fig. 2** EBSD-IPF map (**a**) and corresponding grain boundary map (**b**) of martensitic microstructure with a high fraction of high-angle grain boundaries

charging curves were measured on cylindrical rollers of bearing type 81104 (axial length of 4.5 mm and diameter of 4.5 mm). For charging, the tensile samples were pressure charged in the same experimental setup, wherein two samples can be fit in the pressurized tube.

The hydrogen charging time of 150 h was selected based on a diffusion kinetics estimation using Fick's second law of diffusion for a finite cylindrical specimen. This formulation assumes diffusion time sufficient to achieve equilibrium hydrogen concentration under constant surface concentration conditions. The effective hydrogen diffusion coefficient reported by Kürten et al. [35] for martensitic steel 100Cr6 at 30 °C was adopted.

## 2.3 Slow strain rate tensile tests

Round tensile samples were used for the slow strain rate tensile (SSRT) tests, as shown in Fig. 4. The proportional part of the threaded round tensile sample was manufactured with a diameter of 3 mm and a length of 15 mm and is therefore compliant with ISO 6892. The samples were made of hardened 100Cr6 (760 HV10), which is comparable to the rolling elements. Tensile testing was performed at a constant strain rate of $1 \times 10^{-5}$ $s^{-1}$. The strain rate was selected to highlight the influence of hydrogen, which is the most prominent at low-strain rates [36].

To ensure comparability of hydrogen uptake between the bearing elements and the tensile specimen, the surface area of the tensile samples was polished to a roughness with a *Ra* of 0.01 µm similar to that in the bearing rollers.

The SSRT tests were carried out to quantify the steel's susceptibility to hydrogen embrittlement. The following formula is used for the calculation of the hydrogen embrittlement susceptibility index [27, 36].

$$\mathrm{HEI} = \frac{\varepsilon_0 - \varepsilon_\mathrm{H}}{\varepsilon_0} \tag{1}$$

where $\varepsilon_\mathrm{H}$ and $\varepsilon_0$ represent the elongation at break of the samples with and without hydrogen charging, respectively. An HEI of 0 means that hydrogen has no influence on the material property under investigation, and a value of 1 means that the material characteristic value was no longer measurable [37].

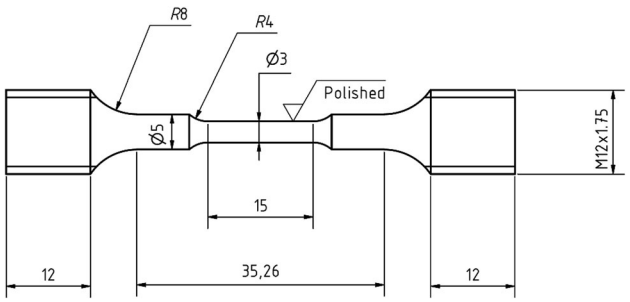


**Fig. 4** Technical drawing of tensile test specimen geometry with M12 thread (Unit: mm)

## 2.4 Thermal desorption mass spectroscopy

For measuring the hydrogen content in the bearing elements, thermal desorption mass spectroscopy (TDMS) was conducted by using a Bruker G4 PHOENIX DH in combination with a mass spectrometer (InProcess Instruments). After hydrogen charging, the samples were stored in liquid nitrogen to avoid hydrogen effusion during idle time. To ensure that there is no contamination on the surface of the sample, the samples were cleaned with acetone in an ultrasonic bath. The cleaned samples were placed in a quartz tube, and the external thermocouple is placed directly on the sample for the most accurate measurement of its temperature. Hydrogen content measurements were carried out by TDMS. The samples were heated up to 800 °C, as fast as possible, using the infrared heater. The effused hydrogen is measured with the mass spectrometer in the carrier gas. The amount of hydrogen is calculated from the TDMS signal using a calibration factor, which is obtained by using 5% hydrogen gas in a calibration routine before the measurement. The calculated value is divided by the sample mass to give the hydrogen content in µg/g.

The solubility of hydrogen can be described using Sievert's law, as shown in Eq. (2) [38].

$$c_\mathrm{H} = k \cdot \sqrt{p_{\mathrm{H}_2}} \tag{2}$$

where $c_\mathrm{H}$ describes the hydrogen concentration dissolved in the material, $10^{-6}$; $p_{\mathrm{H}_2}$ is the external hydrogen gas partial pressure, MPa; and $k$ the Sieverts constant, $10^{-6}$ $\mathrm{MPa}^{-1/2}$, which is material and temperature dependent. Hydrogen concentrations are given in mass fraction ($10^{-6}$, parts per million) throughout the manuscript.

TDMS was chosen as the analysis method because it also provides the opportunity to obtain trapping energies [39, 40]. To determine trapping energies, multiple measurements with various heating rates must be carried out. Different heating rates result in a peak shift of the hydrogen signal, which can be used to determine the energy of release. The slope of the regression line of these data points implemented in a regression plot yields the trapping energy. The following equation was used to determine the trapping energy:

$$\frac{\mathrm{d}\ln(\varphi/T_\mathrm{p}^2)}{\mathrm{d}(1/T_\mathrm{p})} = -\frac{E_\mathrm{A}}{R} \tag{3}$$

where $\varphi$ stands for the heating rate, K/s; $T_\mathrm{p}$ is the temperature at which the peak forms; $R$ is the ideal gas constant; and $E_\mathrm{A}$ is the activation energy of the corresponding

trapping site. Hence, multiplying the slope of the regression line by the ideal gas constant yields the trapping energy. Through deconvolution of the curve, three different peaks are identified [40, 41]. The smoothed curve is approximated with nonlinear curve fitting according to Gaussian peaks, which was used because they achieved the best fit to the curve. Obviously, the peak temperature depends on the applied heating rate. The intensity can be calculated to a desorption rate through multiplication by the calibration factor, which was consistent in the different measurements. The selected heating rates and specimen dimensions ensure reaction-controlled hydrogen desorption, thereby fulfilling the applicability conditions of the Kissinger analysis used to determine trap activation energies.

## 3 Results

### 3.1 Thermal desorption analysis

#### 3.1.1 Hydrogen content

(1) Hydrogen content as function of charging duration (constant pressure).

To establish a time-dependent charging curve for hydrogen, multiple samples were gas pressure charged at a constant pressure of 13 MPa and 90 °C. The testing temperature was chosen based on preliminary tests [3] that resulted in saturation at shorter exposure duration. The hydrogen content was accordingly measured after varying the charging duration. For each duration, the content of five samples was measured.

Figure 5 shows that the virgin samples contained $0.4 \times 10^{-6}$ hydrogen. After charging for 25 h, around $0.75 \times 10^{-6}$ hydrogen was measured, and after 50 h, almost $3 \times 10^{-6}$ was measured. Longer charging durations did not increase the hydrogen content anymore. Charging durations of 75 and 300 h resulted in approximately $3 \times 10^{-6}$ hydrogen, thus indicating saturation in the samples after approximately 50 h. The following saturation equation was numerically fitted from the measurements:

$$C(x) = C_0 + (C_{\max} - C_0) \cdot (1 - \mathrm{e}^{-kx}) \quad (4)$$

where $C(x)$ denotes the hydrogen concentration as a function of the independent variable $x$; $C_0$ represents the initial hydrogen concentration; and $C_{\max}$ corresponds to the saturation concentration reached at large values of $x$. The parameter $k$ is a fitting constant describing the rate at which the concentration approaches the saturation level. The optimal value of $k$ was determined by minimizing the mean squared error (MSE) between the experimental concentration data and the model prediction. In the present study, the variable $x$ represents either the hydrogen charging pressure or the charging duration, depending on the respective evaluation.

(2) Hydrogen content as function of charging pressure (constant duration).

Furthermore, the hydrogen uptake as a function of charging pressure was studied. In Fig. 6, the hydrogen content due to gas pressure charging in a hydrogen atmosphere at different pressures is plotted. For each data point, five samples were analyzed. As shown in Fig. 5, saturation pressure may be achieved after approximately 50 h of gas pressure charging. The samples in these tests were charged for 150 h to ensure uniform hydrogen distribution within the samples prior to testing.

Similarly, the hydrogen content of the virgin samples was found to be approximately $0.4 \times 10^{-6}$. The tests resulted in hydrogen contents of $2.5 \times 10^{-6}$ and

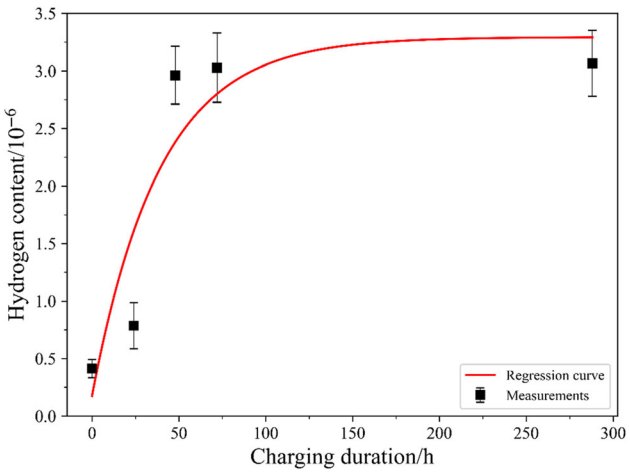


**Fig. 5** Accumulated hydrogen content after pressure charging at 90 °C and 13 MPa pressure for various durations

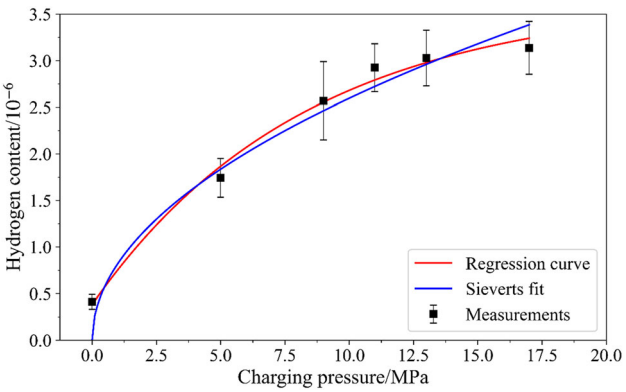


**Fig. 6** Pressure-dependent charging curve after enough charging time to get a steady state, dependent on charging duration

$3.2 \times 10^{-6}$ at 10 and 17 MPa, respectively. The charging curve indicates that increasing hydrogen pressure beyond a certain value results in saturation. Charging pressures of over 10 MPa showed little to no effect on the content of hydrogen in the samples.

In addition to the regression (Eq. (4) described above, a fit according to Sievert (Eq. (2) was also added in Fig. 6, whereby the Sieverts constant was found to be $k = 0.82 \times 10^{-6}$ MPa$^{-1/2}$ (coefficient of determination $r^2 = 0.95$) to achieve the best fit.

(3) Hydrogen effusion.

In this set of experiments, the rate at which the hydrogen effuses (i.e., diffuses out) of the samples stored in ambient laboratory air was investigated. All virgin samples with a hydrogen content of approximately $0.4 \times 10^{-6}$ were gas pressure charged to a saturation content of $3 \times 10^{-6}$ prior to testing. Charging was carried out at 17 MPa and 90 °C for 150 h. The samples were subsequently held at idle in ambient air for varying durations up to 400 h. A reference batch of samples was stored in liquid nitrogen. The hydrogen content decreased in the charged samples as shown in Fig. 7. After 400 h in laboratory air, the hydrogen content decreased to approximately $1.8 \times 10^{-6}$. Samples stored in liquid nitrogen showed much slower effusion rate, with approximately $2.6 \times 10^{-6}$ hydrogen left in the samples after 400 h.

### 3.1.2 Trapping energies

Hydrogen-charged samples with $3 \times 10^{-6}$ hydrogen content were used to measure trapping energies using TDMS. The samples were heated at different rates, and hydrogen desorption rates were obtained from the mass spectrometer signals. Figure 8a shows the hydrogen desorption rate as a function of the testing temperature. The peaks in these figures indicate hydrogen release, and the peak shifts depend on the heating rate. This peak shift may be used to calculate the trap activation energies for the hydrogen traps as detailed in Eq. (3). Besides, Fig. 8b shows the measurement as a function of time; the area under the curve provides the measured hydrogen content. The selected heating rates ensured a moderate signal-to-noise ratio and favorable signal characteristics that permit proper peak separation. Lower heating rates increased noise, thus reducing the possibility of peak identification; whereas higher heating rates resulted in pronounced peak overlap. Therefore, the applied heating rates allowed reliable differentiation of individual desorption peaks.

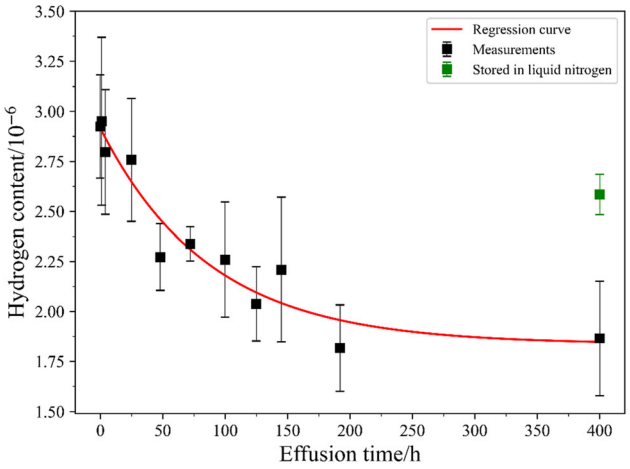


**Fig. 7** Effusion curve after charging samples with 17 MPa for 150 h and leaving samples at laboratory air with comparison to samples kept in liquid nitrogen for same time

The linear regression plot from different heating rates for the measurements is shown in Fig. 9. The plots enable calculating the trap activation energies ($E_A$, see Eq. (3)) resulting from each peak.

The tests were also conducted on samples charged up to $3 \times 10^{-6}$ and subsequently stored in laboratory air for 400 h. The desorption rate and the deconvolution can be seen in Fig. 10.

The measured trapping energies of charged samples and the ones charged and left at laboratory air for 400 h are displayed in Table 2. The peak at the lowest temperature (200–300 °C) is around 30 kJ/mol, the second peak (370–410 °C) is around 45 kJ/mol, and the peak at the highest temperature (440–620 °C) is around 41 kJ/mol.

The hydrogen released at each peak was evaluated at a heating rate of 40 K/min, as shown in Fig. 11. At this heating rate, the peaks can be easily differentiated from one another. The measurement was conducted for charged samples (150 h, 17 MPa) and compared to samples charged (150 h, 17 MPa) and stored at room temperature for 400 h.

The set of measurements indicated the highest hydrogen release occurring at peak 3 (440–620 °C) and the largest difference between charged and charged-and-stored samples.

## 3.2 SSRT tests

The tensile tests with uncharged samples (reference samples) showed a tensile strength of about 2422 ± 42 MPa at a strain of 0.026 ± 0.004 (Fig. 12a). The stress–strain diagrams of the hydrogen-charged samples at 10 and 15 MPa are shown in Fig. 12b; failure of the charged samples does not indicate any appreciable plastic deformation. Moreover, a significant reduction in strength was recorded. The samples charged with hydrogen fail at a mean stress of 1042 ± 25 MPa. The reduction in tensile strength due to hydrogen charging is about 60%. Figure 12a also shows that samples charged at 15 MPa and subsequently idly stored for 400 h in ambient air prior to

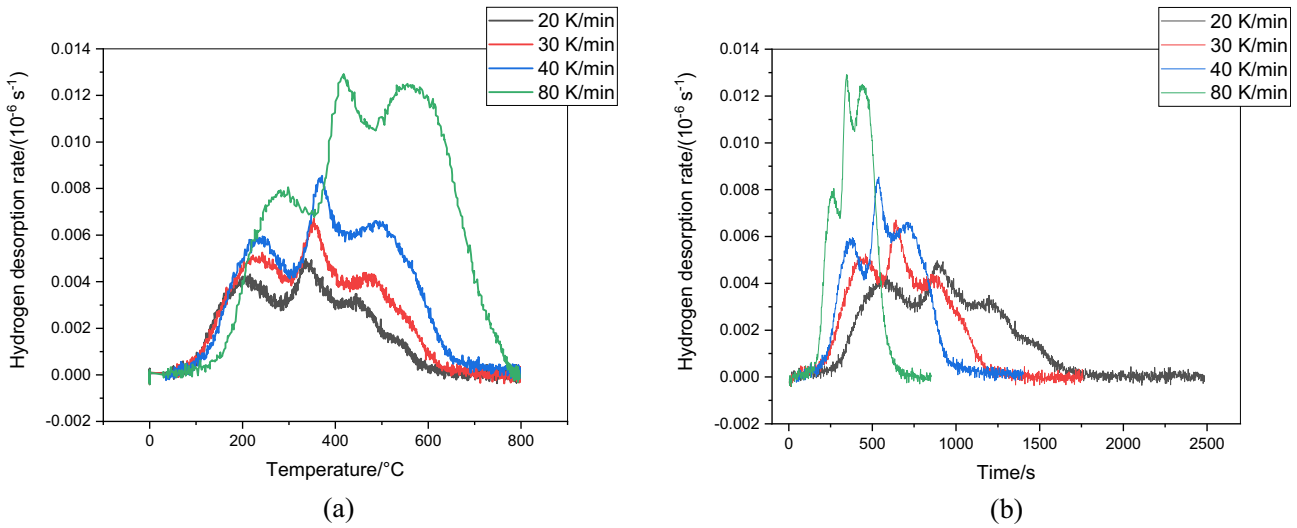


**Fig. 8** Mass spectrometer signals obtained showing hydrogen desorption rate against testing temperature (**a**) and against time (**b**) with samples charged to 3 × 10$^{-6}$

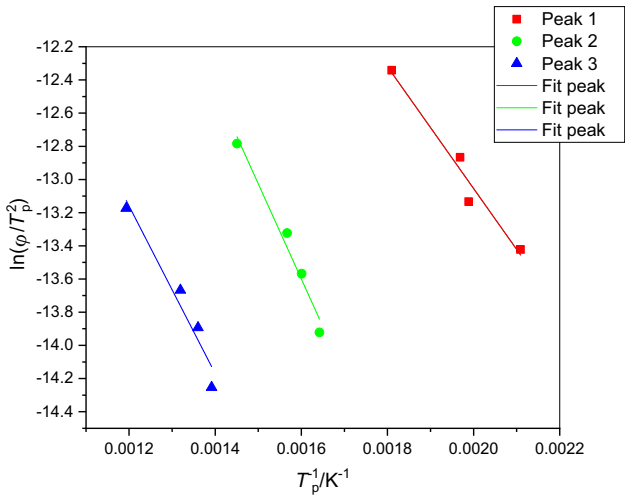


**Fig. 9** Linear regression plot according to Eq. (3) with samples charged to 3 × 10$^{-6}$

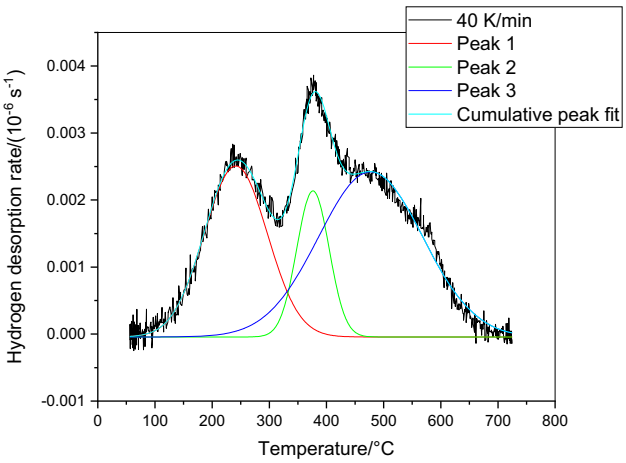


**Fig. 10** Mass spectrometer signals obtained showing hydrogen desorption rate against testing temperature with samples charged to 3 × 10$^{-6}$ and stored in laboratory air for 400 h, heating rate at 40 K/min

conducting the tensile tests (to permit effusion) showed similar ductility and only a slight reduction in tensile strength compared to reference samples.

Furthermore, tensile tests were carried out with different charging pressures, as shown in Fig. 13. Even at lower charging pressures (3 MPa), the behavior is identical to the samples charged with 10 and 15 MPa. The failure occurs prior to any visible plastic strain and at stresses below 1000 MPa. When looking at the tensile samples, the failure occurred at 90° to the direction of loading, which also indicates brittle fracture.

In Fig. 14, the stress at fracture is plotted against the hydrogen content in parts per million (10$^{-6}$) in the tensile samples.

The mean HEI of 0.82 was determined according to Eq. (1). Figure 15 shows the HEI determined from tensile strain measurements after hydrogen charging at different gas pressures. The HEI increases from low to intermediate pressures and approaches a plateau above 5 MPa, while the error bars reflect the propagated experimental uncertainty of the strain data.

The failure of the hydrogen-charged samples appears within the elastic limit at stresses below 1000 MPa. Failure occurred at 90° to the direction of loading, which indicates brittle fracture (Fig. 15).

**Table 2** Measured trapping energies in samples

| Process | Peak 1 (200–300 °C) | | Peak 2 (370–410 °C) | | Peak 3 (440–620 °C) | |
|---|---|---|---|---|---|---|
| | kJ mol$^{-1}$ | $r^2$ | kJ mol$^{-1}$ | $r^2$ | kJ mol$^{-1}$ | $r^2$ |
| 17 MPa charging | −30.5 | 0.95 | −47.7 | 0.96 | −42.0 | 0.92 |
| 17 MPa charging + effusion for 400 h | −32.4 | 0.95 | −42.6 | 0.92 | −40.0 | 0.84 |

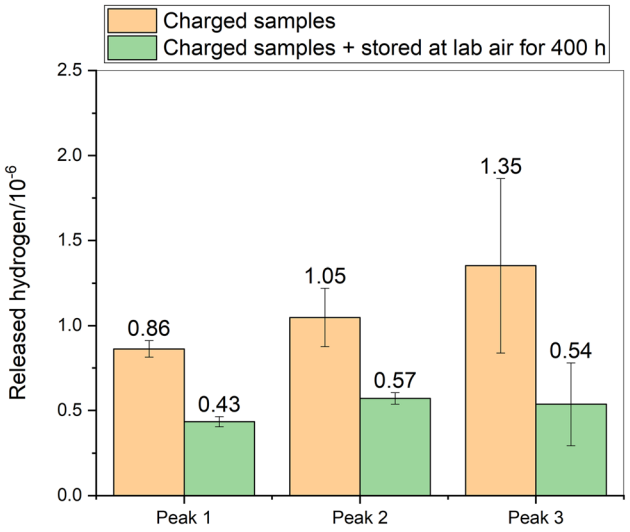


**Fig. 11** Evaluation of individual peaks at a heating rate of 40 K/min for charged samples and samples charged and left idle at room temperature for 400 h after charging, accomplished at 17 MPa

### 3.3 Examination of fracture surfaces with a scanning electron microscope

A fracture surface of a sample charged at 10 MPa for 150 h is shown in Fig. 16. The SEM images were taken at an accelerating voltage of 10 keV. The fracture pattern reveals the fracture origin, which is marked with a circle. Visible fracture lines extend from the marked area to the edge of the sample. Fracture clearly appears to propagate throughout the surface of the sample from the fracture origin.

A closer inspection (500× magnification) of the fracture origin of the 10 MPa sample indicates different structures (Fig. 17). The fracture appears to be mainly intergranular with an adjacent area of ductile fracture with ductile dimples. Also areas of quasi-cleavage fracture can be observed, which are highlighted in the image. The fracture surface appears rather flat and, in both cases, the fracture origin can be identified.

Detailed inspection (magnification of 5,000×) in the hydrogen-charged samples reveals cleaved grain boundaries in the intergranular fracture regions. Furthermore, microductile hairlines, known as crow's feet [25], are visible. The crow's feet are highlighted by the red arrows. The honeycomb structure (lower right corner) indicates residual ductile behavior. In these honeycomb structures, carbides can be found with a diameter of around 300–500 nm (Fig. 18).

The fracture surface of a tensile sample charged with hydrogen at 3 MPa for 150 h is shown in Fig. 19. The

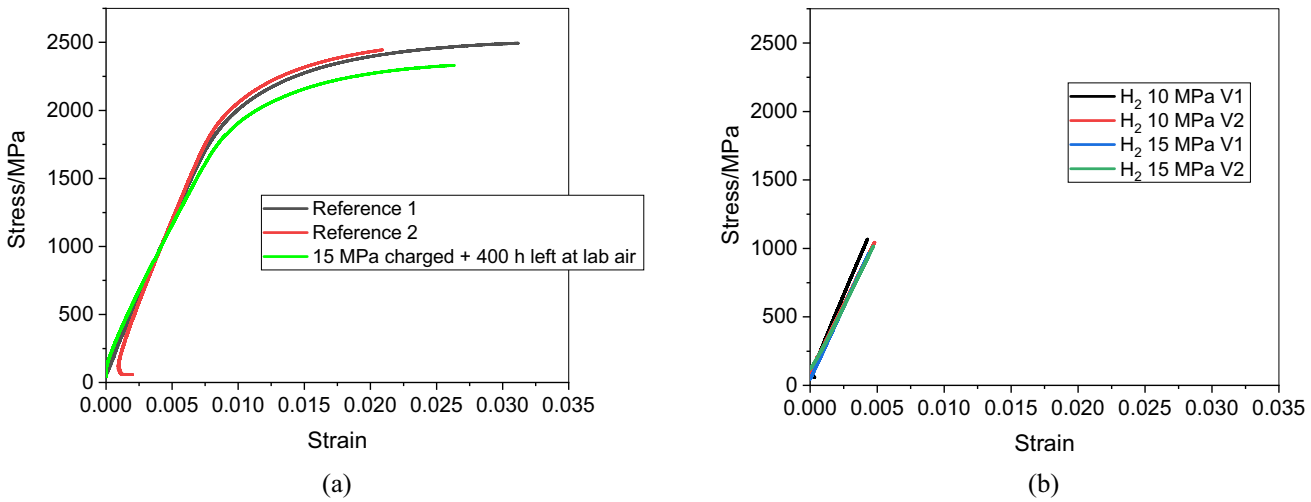


**Fig. 12** Stress–strain diagrams of reference samples (**a**) and charged samples at 10 and 15 MPa hydrogen pressure (**b**)

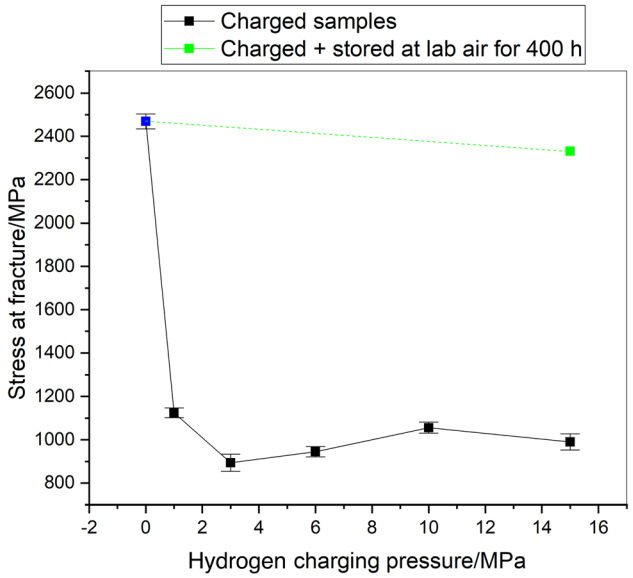


**Fig. 13** Maximum stress at rupture of sample related to hydrogen charging pressure

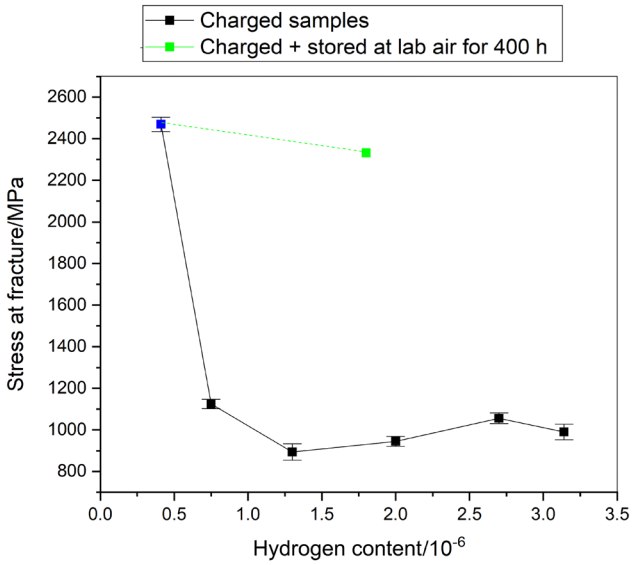


**Fig. 14** Maximum stress at rupture of sample related to hydrogen content

fracture pattern appears similar to the samples charged at 10 MPa. The fracture in both cases exhibits identical patterns with an intergranular fracture origin.

The transition from intergranular fracture to ductile fracture was in the specimen charged with hydrogen at 3 MPa for 150 h and is shown in Fig. 20.

Higher magnification (5000×) image of the grains in the specimen charged with hydrogen at 3 MPa is shown in Fig. 21.

The fracture pattern is similar to that in 10-MPa samples; the fracture is mainly intergranular, and crow's feet identified on the intergranular fracture surface regions and regions of ductile fracture were also visible.

Figure 22 presents an SEM image of the fracture surface showing bright particles within quasi-cleavage facets of a 6 MPa charged sample. Local energy-dispersive spectrometry (EDS) point analyses were performed at two representative locations. At Position 1, the chromium content is approximately 1.5 wt.%, corresponding to the nominal chromium level of 100Cr6 and thus representative of the martensitic matrix. In contrast, Position 2 revealed increased chromium content of approximately 3.2 wt.%, accompanied by a reduced iron fraction. This chromium enrichment is characteristic of (Fe,Cr)-carbides typically present in 100Cr6 bearing steel. Although carbon cannot be reliably quantified by EDS, the compositional contrast confirms that the bright particles correspond to carbide phases. Their frequent occurrence within the quasi-cleavage regions suggests that carbide-related microstructural heterogeneities may contribute to preferred crack initiation sites under hydrogen charging conditions.

The fracture surfaces of uncharged reference samples were also examined (Fig. 23). Fractographic analysis indicated that the fracture originated at a surface-initiated crack (marked with a red circle). The fracture surface is rough, indicating ductile fracture.

The fracture surface of the reference sample, in Fig. 23, reveals rough morphology, indicative of significant ductile fracture. 100Cr6 shows ductile fracture behavior exemplified by void formation and coalescence on the microscopic level. The ridges and valleys in the fracture pattern emphasize the material's ability to undergo plastic yielding prior to fracture.

A closer look at the fracture origin, Fig. 24, shows grain boundaries and ductile dimples. This grain boundary and the pit next to it are located at the center of the crack propagation and could be the origin of the fracture. Overall, the fracture pattern is typical of a high-strength steel, where rough regions and dimples indicate ductile fracture in the matrix and brittle cleavage (flat grain surface) is apparent in the martensitic grain.

A detailed view of the grain surface appearing in Fig. 24 can be seen in Fig. 25. No crow's feet were observed in the uncharged samples even in regions showing intergranular crack growth.

## 4 Discussion

Gas pressure charging of 100Cr6 samples was conducted to construct charging and discharging curves. After 50 h of exposure to hydrogen at 13 MPa, hydrogen content of $3 \times 10^{-6}$ was measured; longer charging durations did not lead to higher hydrogen content, indicating saturation. A

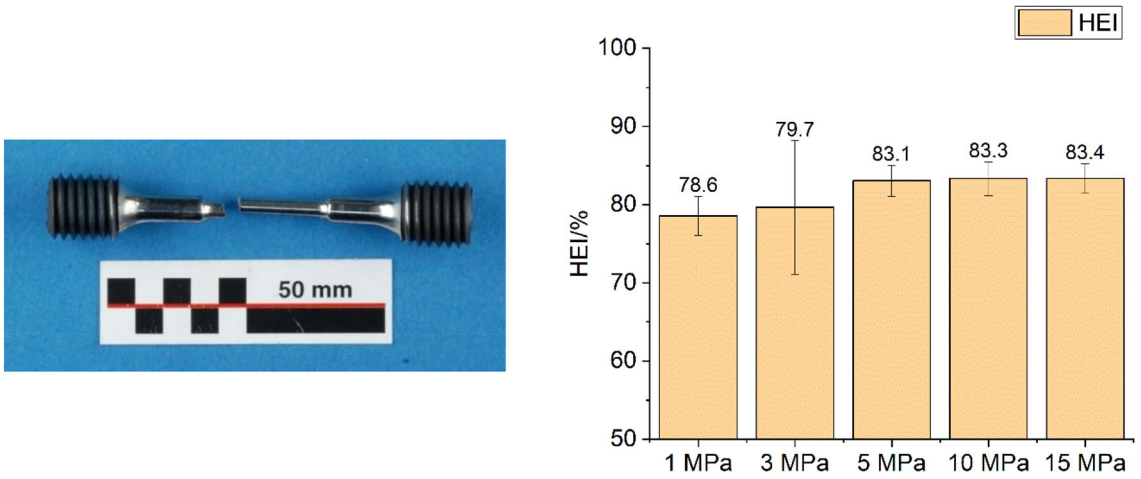


**Fig. 15** Reference tensile sample after testing (left) and HEI as a function of hydrogen gas pressure (right)

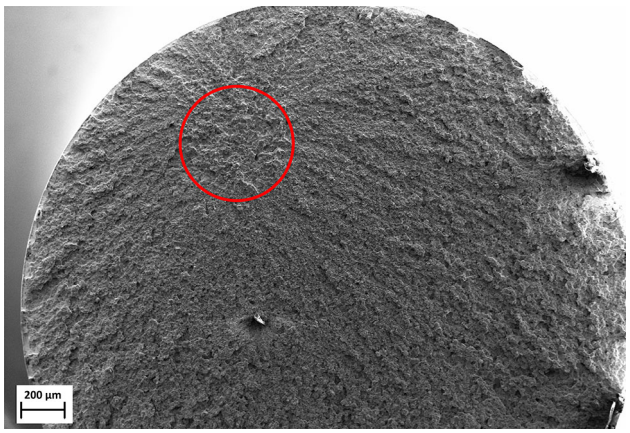


**Fig. 16** SEM image of fracture surface of hydrogen-charged specimen and fracture origin indicated by a circle

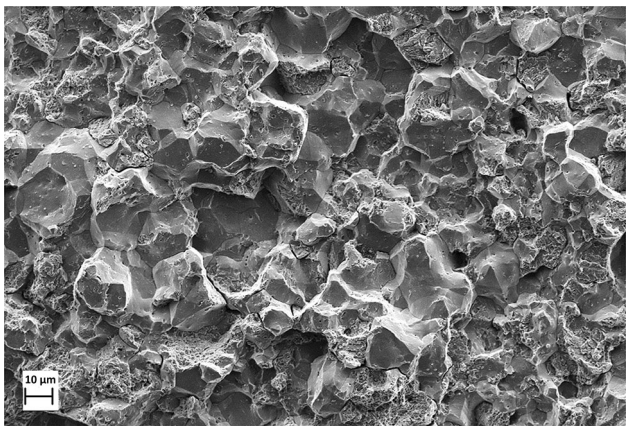


**Fig. 17** SEM image of fracture origin of hydrogen-charged specimen

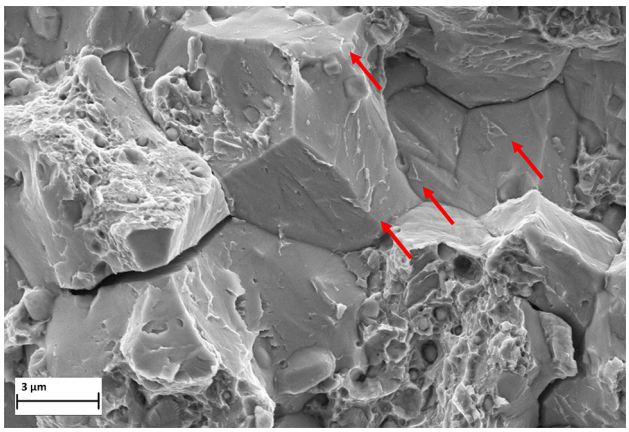


**Fig. 18** SEM image of intergranular fracture region of hydrogen-charged specimen

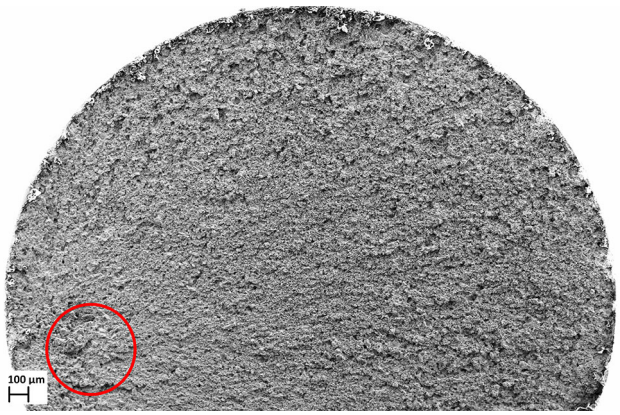


**Fig. 19** SEM image of fracture surface of hydrogen-charged specimen with fracture origin indicated by a circle

pressure-dependent charging curve was thus derived by charging cylindrical bearing components at different charging pressures. The results revealed a maximum hydrogen content of around $3.2 \times 10^{-6}$ at 17 MPa.

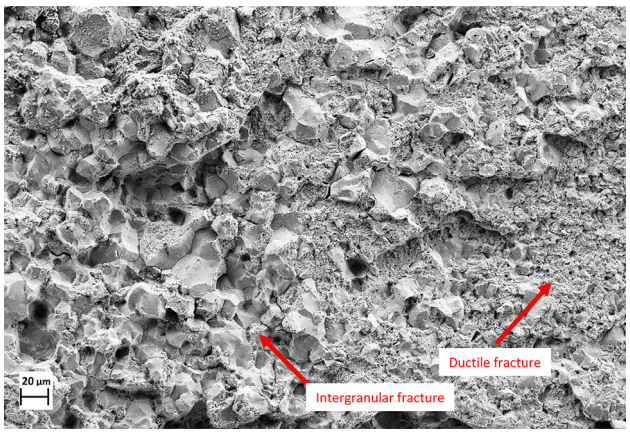


**Fig. 20** SEM image of transition zone from intergranular to ductile fracture of hydrogen-charged specimen

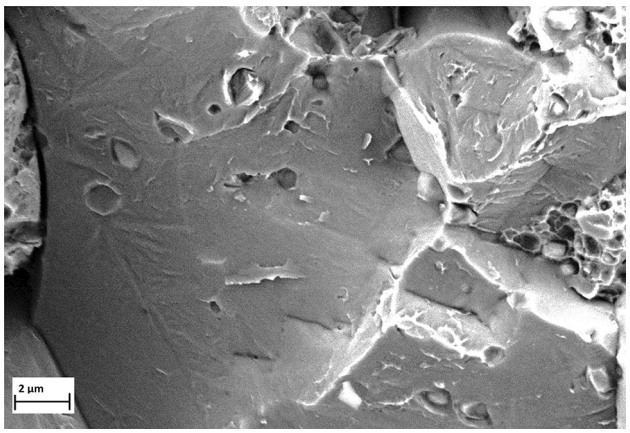


**Fig. 21** SEM image of intergranular fracture region of hydrogen-charged specimen

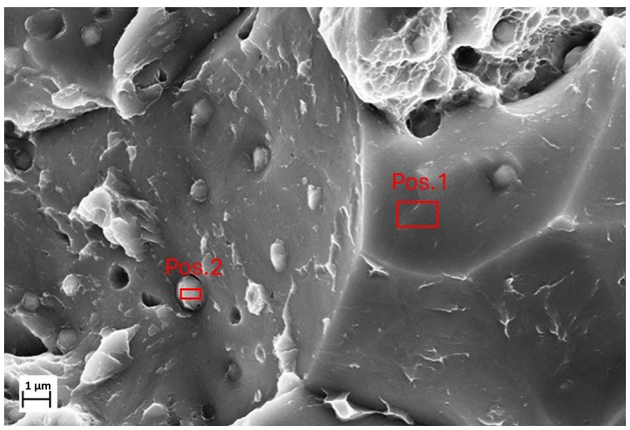


**Fig. 22** SEM image of intergranular fracture region of hydrogen-charged sample

The effusion experiments were conducted on charged samples containing approximately $3 \times 10^{-6}$. Storing the samples in laboratory air for 400 h resulted in a decrease in hydrogen content to approximately $1.8 \times 10^{-6}$. Samples

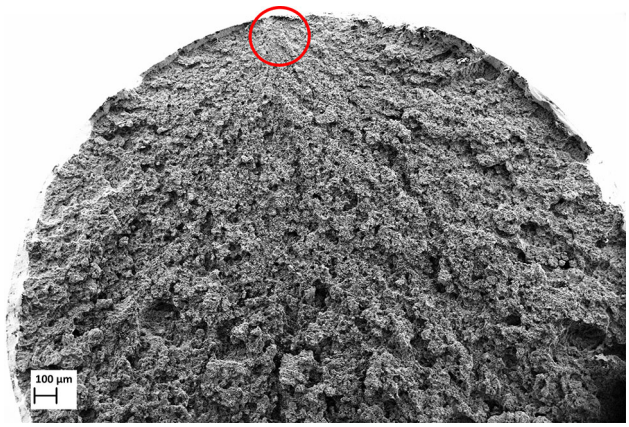


**Fig. 23** SEM image of fracture surface of uncharged reference sample with fracture origin indicated by a circle

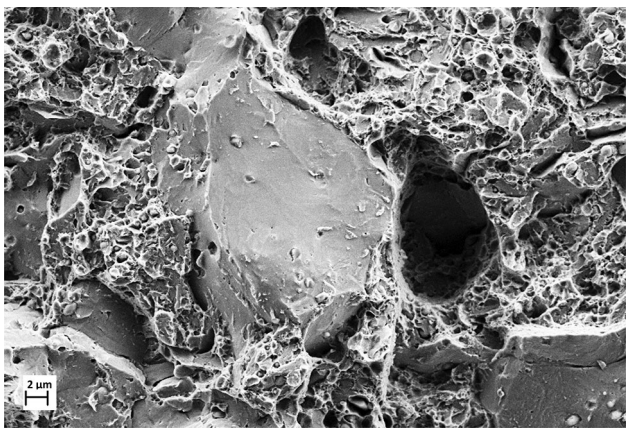


**Fig. 24** SEM image of fracture origin of reference sample

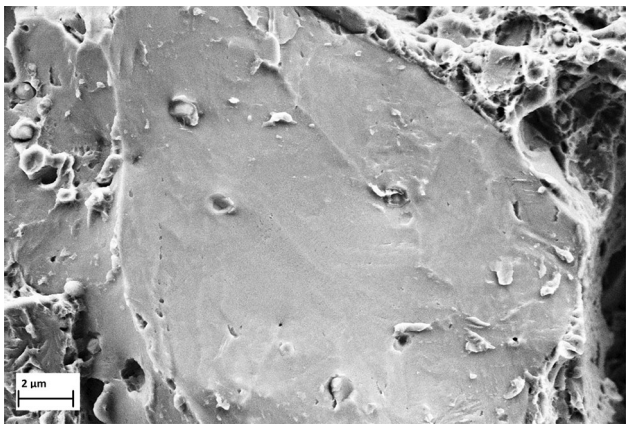


**Fig. 25** SEM image of intergranular fracture region of reference sample

stored in liquid nitrogen at 77 K retained approximately $2.6 \times 10^{-6}$ of hydrogen for the same duration. This confirms that a major portion of absorbed hydrogen will leave the steel if stored at room temperature, indicating weakly trapped hydrogen (i.e., loosely bound in reversible traps

such as dislocations and grain boundaries), which is typically released from steel at room temperature [42].

Compared with the values given in the literature, the value of the Sieverts factor, at $0.82 \times 10^{-6}$ $MPa^{-1/2}$, is significantly higher than the range specified by Sieverts. The upper limit of the range for ferritic steels is just under $0.0316 \times 10^{-6}$ $MPa^{-1/2}$ (or $0.01 \times 10^{-6}$ $bar^{-1/2}$, 1 bar = 100,000 Pa) at a temperature of 90 °C [38]. From this, it can be concluded that hydrogen in the samples is mostly bound in traps, and the trapping model of Oriani [43] or McNabb and Forster [44] applies.

To ensure the transferability of the results from rolling bearing components and tensile samples, a comparable heat treatment process was carried out. The fracture patterns of hydrogen-charged samples tested under tension showed several distinct features. While the fracture surface of the reference (uncharged) samples showed rough morphology, hydrogen-charged samples showed flat smooth fracture surfaces. Although the material is considered brittle (martensitic 100C6), the fracture pattern of the reference samples indicated ductile yielding in Fig. 24. Low ductility can be seen in the stress–strain diagrams, where strain at fracture was less than 0.03 in Fig. 12a. This is in line with the findings of Syniuta and Corrow [45]. Besides, hydrogen-charged samples failed at only 40% of the tensile stress reached by the reference samples. Based on elongation at fracture, the HEI was found to be 0.82, which indicates high susceptibility to hydrogen embrittlement. This is in line with literature findings on hydrogen embrittlement of high-strength steels. Values between 0.70 and 0.85 were reported for concentrations as low as $0.5 \times 10^{-6}$ to $1.0 \times 10^{-6}$ [46–48]. In agreement with the present results, Yanachkov et al. [49] reported for martensitic microstructures a transition from transgranular to intergranular fracture already at hydrogen contents as low as about $0.44 \times 10^{-6}$, indicating that only small amounts of absorbed hydrogen are sufficient to activate grain boundary-controlled failure mechanisms. Hydrogen-charged samples showed dominant intergranular fracture behavior. The reference (uncharged) samples showed small proportion of intergranular fracture regions. These findings suggest that the significant reduction in strength is primarily due to hydrogen-induced grain boundary weakening. This is in line with findings of Okuno and Takai [50] where it was argued that intergranular fracture observed in loading at room temperature was mainly promoted by the reversible stress-assisted accumulation of hydrogen at prior austenite grain boundaries (PAGBs). The high fraction of HAGBs (Fig. 2) in the tensile samples underlined the weakening of grain boundary cohesion, which is in line with findings of Lan et al. [51], where it was shown that HAGBs are more prone to hydrogen embrittlement than LAGBs.

The effusion tests indicated recoverable strength and ductility in charged samples stored idly in ambient air. Tensile strength and strain at fracture had almost been fully restored to a status comparable to that in reference samples. This indicates that reversible trapped, at room temperature diffusible, hydrogen is mostly responsible for the degradation of material properties. In line with analysis carried out by Depover et al. [52], our results indicate that failure in 100Cr6 is governed by martensite-dominated crack initiation, which is exacerbated by diffusible hydrogen. The slight reduction in tensile strength observed in the samples after charging and storing in ambient air is presumably due to the temperature exposure during hydrogen charging (90 °C for 150 h), possibly also caused by the remaining hydrogen content. The reduction in the strength of 100Cr6 bearing steel induced by the hydrogen also explains premature failures that can be observed in rolling bearings in a hydrogen atmosphere and due to hydrogen absorbed through lubricant degradation [3, 4, 53].

The rather low trapping energies (30–48 kJ/mol) measured in the charged samples indicate that mostly reversible traps were filled [54]. The decrease in the hydrogen content of these trapping sites (Fig. 11) indicates that hydrogen can escape again when exposed to laboratory air. The trapping energies measured at 200–300 °C (approximately 30 kJ/mol, peak 1 in Fig. 8 and Table 2) correspond to dislocations [40, 55]. At around 370–400 °C (approximately 45 kJ/mol, peak 2) and 440–650 °C (approximately 41 kJ/mol, peak 3) could either correspond to carbides (most likely chromium carbides) or retained austenite [56]; retained austenite is known to considerably increase the solubility of hydrogen [57]. Literature findings also indicate trapping energies between 43.7 and 49.2 kJ/mol for grain boundaries [58, 59]. Peaks 2 and 3 can therefore be associated with the trapping energy of grain boundaries. This would also account for the intergranular crack growth observed on the fracture surface. Similar results were found in different high-strength martensitic steels under hydrogen influence [50, 51].

The experimental results demonstrate clear correlation between the hydrogen content and mechanical property degradation; even limited hydrogen uptake, achieved through low-pressure charging for short durations (Figs. 5 and 6), results in a pronounced degradation in strength (Fig. 14). The observed mechanical recovery following ambient air storage is attributed to the effusion of mobile (diffusible and weakly trapped) hydrogen, thereby identifying it as the principal cause of strength degradation. TDMS measurement data further highlight the role of hydrogen trapping, showing that strongly trapped hydrogen (corresponding to high-temperature effusion peaks, Fig. 8) exert only a minor influence on strength.

That the third peak at approximately 440–650 °C has a lower activation energy than the second peak (at lower temperature) could be due to more complicated processes that cannot be explained by the method used [60, 61].

The amount of hydrogen at each of these traps is reduced by idle storing in ambient air. The overall reduction in hydrogen content makes it difficult to draw conclusions regarding the nature of traps that mostly influence the tensile strength of steel.

Hydrogen embrittlement is driven by synergistic effects of HEDE and HELP. Diffusible hydrogen is known to be present in high concentrations at grain boundaries, thus leading to HEDE through weakened cohesion of grain boundaries and resulting in intergranular fracture. Additionally, enhanced dislocation mobility due to the HELP causes dislocations to pile-up at the grain boundaries [22, 62, 63].

## 5 Summary

1. The hydrogen content recorded by gas charging of cylindrical roller bearing elements no longer shows any major change above 10 MPa, allowing a steady state to be measured just over $3 \times 10^{-6}$.
2. The tensile tests of the hydrogen-charged samples have shown that even a charging of only 3 MPa leads to a drastic reduction in strength.
3. Regardless of the charging pressure, a tensile strength of around 40% of the strength in the unloaded state was measured.
   a. The HEI considering the strain at rupture was determined to 0.82. Therefore, the hardened 100Cr6 steel is very susceptible to hydrogen embrittlement.
   b. This demonstrates that even low concentrations of hydrogen can have a critical impact on the material's strength and may account for premature bearing failures.
4. Fractographic analysis confirmed characteristic features of hydrogen embrittlement, including intergranular fracture and "crow's feet" patterns.
5. Charging the tensile sample with 15 MPa hydrogen gas and leaving them at laboratory air for 400 h reverse the reduction in tensile strength, and the behavior of the sample is again the same as the uncharged condition.
6. The measurement of the trapping energies showed that the trapping energies are around 30 kJ/mol which are assumed to correspond to dislocations and at 40–47.7 kJ/mol corresponding to the (high-angle) grain boundaries, but could also correspond to the chromium carbides or retained austenite.
7. The correlation of the elevated hydrogen content and the drastic reduction in the tensile strength of the bearing steel could be demonstrated. The reduction in strength is reversed by the effusion of diffusible hydrogen.

**Acknowledgements** The authors gratefully acknowledge the financial support of the German Research Foundation (DFG) within the project *CoLifeHy* (Grant No. 450828000).

**Funding** Open Access funding enabled and organized by Projekt DEAL.

**Data availability** Due to privacy restrictions, the data underlying this study can be obtained from the corresponding author upon request.

## Declarations

**Conflict of interest** All authors declare that there is no conflict of interest.



## References

[1] M. Alexander Stopher, P.E.J. Rivera-Diaz-del-Castillo, Mater. Sci. Technol. 32 (2016) 1184–1193.
[2] N. Kino, JSAE Rev. 24 (2003) 289–294.
[3] M. Baur, I. Khader, D. Kürten, T. Schieß, A. Kailer, M. Dienwiebel, Lubricants 12 (2024) 311.
[4] D. Kürten, I. Khader, R. Raga, P. Casajús, N. Winzer, A. Kailer, R. Spallek, M. Scherge, Eng. Fail. Anal. 99 (2019) 330–342.
[5] M. Kohara, T. Kawamura, M. Egami, Tribol. Trans. 49 (2006) 53–60.
[6] M.H. Evans, A.D. Richardson, L. Wang, R.J.K. Wood, Wear 306 (2013) 226–241.
[7] Y. Sun, Y.F. Cheng, Int. J. Hydrogen Energy 46 (2021) 34469–34486.
[8] A. Trautmann, G. Mori, B. Loder, BHM Berg Und Hüttenmännische Monatsh 166 (2021) 450–457.
[9] P. Gong, A. Turk, J. Nutter, F. Yu, B. Wynne, P. Rivera-Diaz-del-Castillo, W.M. Rainforth, Acta Mater. 223 (2022) 117488.
[10] E.D. Fan, S.Q. Zhang, D.H. Xie, Q.Y. Zhao, X.G. Li, Y.H. Huang, Int. J. Miner. Metall. Mater. 28 (2021) 249–256.
[11] M. Pinson, K. Nikolic, H. Springer, T. Depover, K. Verbeken, Procedia Struct. Integr. 42 (2022) 471–479.
[12] P. Roffey, J Fail. Anal. And Preven. 15 (2015) 161–167.
[13] T.T. Nguyen, J. Park, S.H. Nahm, N. Tak, U.B. Baek, Int. J. Hydrogen Energy 44 (2019) 28031–28043.
[14] Y. Mine, T. Kimoto, Corros. Sci. 53 (2011) 2619–2629.

[15] M.L. Martin, M. Dadfarnia, A. Nagao, S. Wang, P. Sofronis, Acta Mater. 165 (2019) 734–750.
[16] D. Wang, X. Lu, D. Wan, X. Guo, R. Johnsen, Mater. Sci. Eng. A 802 (2021) 140638.
[17] Z. Tarzimoghadam, M. Rohwerder, S.V. Merzlikin, A. Bashir, L. Yedra, S. Eswara, D. Ponge, D. Raabe, Acta Mater. 109 (2016) 69–81.
[18] M.B. Djukic, G.M. Bakic, V. Sijacki Zeravcic, A. Sedmak, B. Rajicic, Eng. Fract. Mech. 216 (2019) 106528.
[19] M.B. Djukic, V.S. Zeravcic, G. Bakic, A. Sedmak, B. Rajicic, Procedia Mater. Sci. 3 (2014) 1167–1172.
[20] X. Li, X. Ma, J. Zhang, E. Akiyama, Y. Wang, X. Song, Acta Metall. Sin. (Engl. Lett.) 33 (2020) 759–773.
[21] P. Novak, R. Yuan, B.P. Somerday, P. Sofronis, R.O. Ritchie, J. Mech. Phys. Solids 58 (2010) 206–226.
[22] D.H. Kim, M. Moallemi, K.S. Kim, S.J. Kim, J. Mater. Res. Technol. 20 (2022) 18–25.
[23] X. Xing, J. Gou, F. Li, Y. Zhang, J. Cheng, Y. Wang, J. Liu, G. Cui, Z. Li, P. Zhang, X. Luo, B. Wang, Int. J. Hydrogen Energy 46 (2021) 36528–36538.
[24] A. Neidel, B. Fischer, T. Ullrich, Pract. Metallogr. 51 (2014) 734–744.
[25] M.A.A. Mohd Salleh, D. Sebayang, D.I.C. Syahril, A. Sitompul, N.Z. Noriman, S.R. Shamsudin, Adv. Mater. Res. 795 (2013) 455–458.
[26] G. Álvarez, Z. Harris, K. Wada, C. Rodríguez, E. Martínez-Pañeda, Addit. Manuf. 78 (2023) 103834.
[27] N. Zhao, Q. Zhao, Y. He, R. Liu, W. Zheng, W. Liu, Y. Zhang, J. Mater. Res. Technol. 15 (2021) 6883–6900.
[28] T. Depover, D. Pérez Escobar, E. Wallaert, Z. Zermout, K. Verbeken, Int. J. Hydrogen Energy 39 (2014) 4647–4656.
[29] L.B. Peral, A. Díaz, C. Colombo, J. Alegre, I.I. Cuesta, Int. J. Hydrogen Energy 63 (2024) 657–667.
[30] E. Koren, C.M.H. Hagen, D. Wang, X. Lu, R. Johnsen, J. Yamabe, Corros. Sci. 215 (2023) 111025.
[31] I. Moro, L. Briottet, P. Lemoine, E. Andrieu, C. Blanc, G. Odemer, Mater. Sci. Eng. A 527 (2010) 7252–7260.
[32] E. Malitckii, Y. Yagodzinskyy, P. Vilaça, Mater. Sci. Eng. A 760 (2019) 68–75.
[33] Y. Murakami, T. Kanezaki, P. Sofronis, Eng. Fract. Mech. 97 (2013) 227–243.
[34] V. Šmeļova, A. Schwedt, L. Wang, W. Holweger, J. Mayer, Int. J. Fatigue 98 (2017) 142–154.
[35] D. Kürten, I. Khader, A. Kailer, Mater. Corros. 71 (2020) 918–923.
[36] T. Hojo, R. Kikuchi, H. Waki, F. Nishimura, Y. Ukai, E. Akiyama, ISIJ Int. 58 (2018) 751–759.
[37] F. Aiello, M. Beghini, C.M. Belardini, L. Bertini, G. Macoretta, B.D. Monelli, R. Valentini, Corros. Sci. 222 (2023) 111357.
[38] A. Sieverts, Z. Für Phys. Chem. 77U (1911) 591–613.
[39] L. Simoni, T. Falcade, D.C.F. Ferreira, C.E.F. Kwietniewski, Int. J. Hydrogen Energy 46 (2021) 25738–25751.
[40] A. Zafra, L.B. Peral, J. Belzunce, Int. J. Hydrogen Energy 45 (2020) 31225–31242.
[41] J. Yamabe, M. Yoshikawa, H. Matsunaga, S. Matsuoka, Int. J. Fatigue 102 (2017) 202–213.
[42] Y.S. Chen, C. Huang, P.Y. Liu, H.W. Yen, R. Niu, P. Burr, K.L. Moore, E. Martínez-Pañeda, A. Atrens, J.M. Cairney, Int. J. Hydrogen Energy 136 (2025) 789–821.
[43] R.A. Oriani, Acta Metall. 18 (1970) 147–157.
[44] A. McNabb, P.K. Foster, Institute of Metals Division-A New Analysis of the Diffusion of Hydrogen in Iron and Ferritic Steels, The American Institute of Mining, Metallurgical, and Petroleum Engineers, 1963.
[45] W.D. Syniuta, C.J. Corrow, Wear 15 (1970) 171–186.
[46] K. Takasawa, R. Ikeda, N. Ishikawa, R. Ishigaki, Int. J. Hydrogen Energy 37 (2012) 2669–2675.
[47] S. Cho, G.I. Kim, S.J. Ko, J.S. Yoo, Y.S. Jung, Y.H. Yoo, J.G. Kim, Materials 15 (2022) 3406.
[48] S. Lynch, Corros. Rev. 30 (2012) 105–123.
[49] B. Yanachkov, Y. Mourdjeva, K. Valuiska, V. Dyakova, K. Kolev, J. Kaleicheva, R. Lazarova, I. Katzarov, Metals 14 (2024) 1340.
[50] K. Okuno, K. Takai, Acta Mater. 259 (2023) 119291.
[51] X. Lan, K. Okada, R. Ueji, A. Shibata, Scripta Mater. 274 (2026) 117157.
[52] T. Depover, D. Wan, D. Wang, A. Barnoush, K. Verbeken, Mater. Charact. 167 (2020) 110493.
[53] A.D. Richardson, M.H. Evans, L. Wang, R.J.K. Wood, M. Ingram, Tribol. Lett. 66 (2018) 4.
[54] S. Sagar, M.H.F. Sluiter, P. Dey, Int. J. Hydrogen Energy 50 (2024) 211–223.
[55] L.B. Peral, Z. Amghouz, C. Colombo, I. Fernández-Pariente, Theor. Appl. Fract. Mech. 110 (2020) 102771.
[56] B.A. Szost, R.H. Vegter, P.E.J. Rivera-Díaz-del-Castillo, Metall. Mater. Trans. A 44 (2013) 4542–4550.
[57] K.G. Solheim, J.K. Solberg, J. Walmsley, F. Rosenqvist, T.H. Bjørnå, Eng. Fail. Anal. 34 (2013) 140–149.
[58] K. Ono, M. Meshii, Acta Metall. Mater. 40 (1992) 1357–1364.
[59] R. Sato, K. Takai, Scripta Mater. 228 (2023) 115339.
[60] S. Vyazovkin, Phys. Chem. Chem. Phys. 18 (2016) 18643–18656.
[61] R. Kirchheim, Metall. Mater. Trans. A 47 (2016) 672–696.
[62] S.K. Dwivedi, M. Vishwakarma, Int. J. Hydrogen Energy 43 (2018) 21603–21616.
[63] O. Barrera, D. Bombac, Y. Chen, T.D. Daff, E. Galindo-Nava, P. Gong, D. Haley, R. Horton, I. Katzarov, J.R. Kermode, C. Liverani, M. Stopher, F. Sweeney, J. Mater. Sci. 53 (2018) 6251–6290.